ORA Mathematics, 1(1), e2026005
DOI: 10.XXXXX/oramath.e2026005
Received: 22 April 2026
Revised: 04 May 2026
Accepted: 07 May 2026
Published: 08 May 2026

RESEARCH ARTICLE

Fractional-order bilinear feature network for exact solutions of the (1+1)-dimensional Caudrey–Dodd–Gibbon equation

Mueen ud Din*

Riphah College of Computing, Riphah International University, Faisalabad, Pakistan.

* **Correspondence:** Email: mueen80@gmail.com

Abstract: The fifth-order dispersive nonlinear wave model for plasma magnetosonic waves and soliton propagation in optical fibers is the (1+1)-dimensional Caudrey-Dodd-Gibbon (CDG) equation. The equation has many solution structures, but recovering them in exact closed form is an analytical difficulty. The bilinear neural network methods used are based on regular polynomial feature augmentation, which limits their ability to handle memory effects and anomalous dispersion when the CDG equation is extended to fractional order. Our Fractional-Order Bilinear Feature Network fills this gap. The concept is to replace ordinary monomial features x^2, t^2, and xt with conformable fractional-order features x^α, t^α, and $(xt)^{\alpha/2}$ with order $\alpha \in (0,$ This expands the trial function's representation while maintaining Hirota bilinear machinery's symbolic accuracy. Maple imposes algebraic zero-residual constraints on the fractional system and finds four closed-form precise solutions for single- and double-hidden-layer network architectures. Comparative simulations in integer and fractional regimes demonstrate the impact of α on solitons' amplitude, propagation speed, and energy localization. Three-dimensional surface plots, contour diagrams, density maps, and multi-time curve graphs show dynamics. On the domain $x, t \in (-30, 30)$, numerical checks reveal 2-4% enhancements in peak amplitude and wave-front sharpness fidelity over the conventional integer-order baseline, with no analytical error. The framework gives an easy technique to create accurate solutions of fractional CDG variations arising in plasma physics, quantum field theory and nonlinear optics.

Keywords: Caudrey–Dodd–Gibbon equation; Fractional-Order Bilinear Feature Network (FOBFN); conformable fractional derivative; Hirota bilinear method; exact soliton solutions; symbolic computation; nonlinear wave dynamics

Mathematics Subject Classification: 35R11, 65M60, 35Q53

1. Introduction

Nonlinear partial differential equations (NLPDEs) are widely used as mathematical models for wave phenomena in fluid mechanics, optical fiber communication and plasma physics. Among the many equations that populate this landscape, the (1+1)-dimensional Caudrey–Dodd–Gibbon (CDG) equation has attracted special attention. It is a member of the fifth-order tier of the Korteweg–de Vries (KdV) hierarchy and the soliton solutions it possesses, along with their interaction dynamics, have real-world implications for the propagation of magnetosonic waves and for the way optical pulses travel along a fiber [13, 22, 27]

Written out explicitly, the CDG equation takes the form

$$u_t + u_{xxxxx} + 30\,u_{xxx} + 30\,u_x u_{xx} + 180\,u_x^2 u_{xx} = 0, \tag{1}$$

where $u = u(x,t)$ denotes the wavefield. Eq. (1) belongs to an integrable hierarchy which was first discovered by Caudrey, Dodd and Gibbon [14] and the integrability has been confirmed by Painlevé analysis, Lax pair construction and derivation of conservation laws [5, 15].

There are quite a few exact solution methods for the equation (1). The Hirota bilinear approach along with a well selected ansatz yields breather waves and lump-periodic structures [7]. Methods based on expansion ideas such as the (G'/G)-expansion and the modified simple equation technique [6] achieve traveling wave solutions in terms of trigonometric or hyperbolic functions. In the case of non-integrability, the variational iteration method and the Khater-II method are useful semi-analytical alternatives [1]. The solution families have been extended to fractional and higher-dimensional settings using Lie group analysis and the Laplace residual power series [3, 4, 22].

Fractional extensions of Equation (1) have been the subject of ongoing research interest as they can model hereditary and memory effects that cannot be modeled by integer-order models. The fractional CDG equation has been analytically presented by Singh et al. [15] by using Adomian decomposition. Fathima et al. [5] have studied the propagation of magnetoacoustic waves using non-singular kernel derivatives. In [13], Shakeel et al. constructed soliton families for the time-fractional Caudrey–Dodd–Gibbon–Sawada–Kotera (CDGSK) system via Painlevé analysis, and in [8], Jhangeer et al. used a performance analysis to measure the effect of the fractional derivative order on wave profiles. Rao et al. [12] employed a numerical method for the time-fractional CDGSK equation, and Deng et al. [2] used a local fractional iterative scheme for a Kaeda variant. Both the optimized Caputo power series of Eriqat et al. [4] and the new closed-form method of El-Ajou and Burqan [3] emphasize that fractional operators produce truly new dynamical behavior that cannot be reproduced in the integer case.

For neural networks, the bilinear neural network method (BNNM) was a major breakthrough because it used Hirota operators and symbolic computation to obtain an exact analytical solution, not just a numerical solution [10, 17]. This idea was further extended by Ye et al. [20] through the conformable bilinear neural network method which employs the conformable derivative definitions to obtain exact solutions for time-fractional NLPDEs that the classical BNNM cannot solve. Multivariate bilinear neural networks have further expanded the solution space by allowing hidden neurons to depend on multiple variables at the same time [10]. Amidst all this activity, no one has yet succeeded in establishing a unified framework that systematically replaces the polynomial features of integer order in a bilinear neural network with conformable fractional-order ones, while guaranteeing symbolic exactness, specifically for the CDG equation family.

Some recent papers have opened new directions on the CDG equation itself. Sun et al. [16] obtained the resonant and rogue wave solutions for the (2+1)-dimensional CDG equation. Wang et al. [18] constructed the controllable transformed waves for the variable-coefficient Caudrey-Dodd-Gibbon-Kotera-Sawada (CDGKS) system. Using modern analytical tools, Kaur et al. [9] studied the CDGSK equation. Resonance Y-shape solitons for a (2+1)-dimensional generalized CDGKS system were reported by Ma et al. [11]. The growing role of operator learning in this area is illustrated by Wang et al. [19] who showed data-driven soliton reconstruction for the

fifth-order CDG equation using the HyperFNO model.

In this work, the Fractional-Order Bilinear Feature Network (FOBFN) is introduced. The key step is to replace the input augmentation set $\{x^2, t^2, xt\}$ by the conformable fractional features $\{x^\alpha, t^\alpha, (xt)^{\alpha/2}\}$ for a tunable order $\alpha \in (0, 2)$. At $\alpha = 2$ the method reduces exactly to the integer-order baseline. Therefore, every classical BFESCNN solution is retrieved automatically. Away from 2, the trial function acquires sub-quadratic spatial correlations that are characteristic of anomalous wave dispersion. In Maple, symbolic computation imposes the corresponding algebraic zero-residual conditions and we obtain four families of exact solutions for the CDG equation. Then, a comparative simulation study over $\alpha \in \{1.0, 1.4, 1.8, 2.0\}$ is carried out to quantitatively demonstrate how fractional order alters the morphology, peak amplitude, and propagation speed of the solution.

The paper is organized as follows . Section 2 builds the FOBFN framework, covering the Hirota bilinear form of Equation (1), the construction of the fractional features, the five-step algorithmic pipeline, and comparison tables that place the method relative to existing approaches. Four exact solutions of single-hidden-layer and double-hidden-layer FOBFN architectures are presented in Section 3 with graphical analysis. The comparative simulation study with quantitative metrics over fractional orders is reported in Section 4. The physical meaning of the fractional parameter is discussed in Section 5. The main conclusions are summarized in Section 6.

2. The FOBFN Framework

2.1. Hirota Bilinear Form Of The CDG Equation

Introducing the auxiliary function $f = f(x, t)$ and applying the Hirota bilinear transformation

$$u(x, t) = 2\big(\ln f\big)_{xx} \tag{2}$$

converts Equation (1) into the bilinear form

$$\big(D_t D_x + D_x^6\big) f \cdot f = 0. \tag{3}$$

In Equation (3), the symbol $D_t^m D_x^n$ stands for the Hirota bilinear operator

$$D_t^m D_x^n f \cdot g = \sum_{k=0}^{m} \sum_{l=0}^{n} (-1)^k \binom{m}{k} \binom{n}{l} \frac{\partial^{m-k} f}{\partial t^{m-k}} \frac{\partial^{n-l} f}{\partial x^{n-l}} \cdot \frac{\partial^k g}{\partial t^k} \frac{\partial^l g}{\partial x^l}. \tag{4}$$

Expanding Equation (3) term by term gives

$$f_t f_x - f_x f_t + f_{xxxxxx} f - 6 f_{xxxxx} f_x + 15 f_{xxxx} f_{xx} - 10 f_{xxx}^2 = 0. \tag{5}$$

Every trial function f that we write down must satisfy Equation (5) identically; the physical solution is then recovered through Equation (2).

2.2. Conformable Fractional Feature Construction

Standard bilinear neural network methods enrich the input pair (x, t) with the polynomial set $\{x^2, t^2, xt\}$. In the FOBFN, this set is replaced by conformable fractional features indexed by the order $\alpha \in (0, 2)$.

Definition 2.1. Let $\alpha \in (0, 1]$. For a positive real variable $s > 0$, the conformable fractional power feature at order α is

$$\Psi_\alpha(s) = s^\alpha, \qquad s \in \mathbb{R}^+. \tag{6}$$

For $\alpha \in (1, 2)$, the cross-term feature is $(xt)^{\alpha/2}$, which interpolates smoothly between xt when $\alpha = 2$ and $(xt)^{1/2}$ when $\alpha = 1$.

Each neuron in the first hidden layer therefore receives the five-component input vector

$$\mathbf{z} = \left(x,\ t,\ x^\alpha,\ t^\alpha,\ (xt)^{\alpha/2}\right)^\top, \tag{7}$$

in place of the classical integer-order vector $\mathbf{z}_{\text{int}} = (x, t, x^2, t^2, xt)^\top$. When $\alpha = 2$, Equation (7) reduces to $\mathbf{z}_{\text{int}}$ exactly, so all classical BFESCNN solutions are automatically recovered as a particular case of the FOBFN.

The pre-activation for the i-th neuron in the first hidden layer is

$$\xi_i = \omega_{x,i}\, x + \omega_{t,i}\, t + \omega_{x^\alpha,i}\, x^\alpha + \omega_{t^\alpha,i}\, t^\alpha + \omega_{(xt)^{\alpha/2},i}\, (xt)^{\alpha/2} + b_i, \qquad i = 1, 2, \tag{8}$$

where $\omega_{\cdot,i}$ are real weight parameters and b_i are real biases.

2.3. Network Architectures

We study two architectures that mimic the single- and double-hidden-layer structure of the integer-order baseline, enabling a direct comparison.

2.3.1. FOBFN 2-5-2-1 Architecture. One Hidden Layer: The input layer is fed with the five-component vector (7). In the hidden layer, two neurons apply activation functions Φ_1 and Φ_2 to ξ_1 and ξ_2 respectively. The output layer combines them as

$$f = w_{1,f}\, \Phi_1(\xi_1) + w_{2,f}\, \Phi_2(\xi_2) + b_3. \tag{9}$$

Two activation pairs are examined. Case 1 takes $\Phi_1(\xi) = \xi^2$ and $\Phi_2(\xi) = \xi^2$; Case 2 takes $\Phi_1(\xi) = \operatorname{sech}(\xi)$ and $\Phi_2(\xi) = \xi^2$.

2.3.2. Double-Hidden-Layer FOBFN 2-5-2-2-1 Architecture: An intermediate layer adds neurons ξ_3 and ξ_4 through

$$\xi_3 = w_{1,3}\, \xi_1 + w_{2,3}\, \xi_2 + b_3, \qquad \xi_4 = w_{1,3}\, \xi_1 + w_{2,3}\, \xi_2 + b_4, \tag{10}$$

and the output layer produces

$$f = w_{3,f}\, \Phi_3(\xi_3) + w_{4,f}\, \Phi_4(\xi_4) + b_5. \tag{11}$$

Case 1 uses $\Phi_3(\xi) = \xi^2$ and $\Phi_4(\xi) = \xi^2$; Case 2 uses $\Phi_3(\xi) = \xi^2$ and $\Phi_4(\xi) = \operatorname{sech}(\xi)$.

2.4. Five-Step Algorithmic Pipeline

The FOBFN solution procedure proceeds through five steps.

Step 1. Apply transformation (2) to Equation (1) to arrive at the bilinear form (5).

Step 2. Build the fractional-feature trial function f from Equations (8)–(9) or (11), then substitute it into Equation (5).

Step 3. Expand the substituted expression and gather the coefficients of every independent monomial $x^\beta t^\gamma$ and every derivative of Φ:

$$x^{\beta_1} t^{\gamma_1},\ x^{\beta_2} t^{\gamma_2},\ \ldots,\ \Phi'(\xi_i),\ \Phi''(\xi_i),\ \ldots \tag{12}$$

Setting each gathered coefficient to zero produces a nonlinear algebraic system in the weights ω and biases b.

Step 4. Solve the algebraic system in Maple. Each nonzero solution branch gives explicit values for all parameters.

Step 5. Insert the solved parameters back into Equation (2) to obtain the exact solution $u(x,t)$. Verify correctness by substituting u directly into the left-hand side of Equation (1) and checking that Maple returns zero.

2.5. Comparison With Related Methods

Table 1 compares the FOBFN with integer-order BFESCNN, Hirota bilinear method, Physics-Informed Neural Networks (PINNs), and fractional analytical methods in six dimensions.

Table 1. Comparison of FOBFN with related methods across six evaluation dimensions.

Dimension	**FOBFN (This study)**	**BFESCNN (Integer)**	**Hirota / Analytical**	**PINNs / Fractional Numerical**
Solution type	Exact analytical; fractional and integer CDG families	Exact analytical; integer CDG only	Exact analytical; specific solution classes	Approximate numerical; any PDE
Feature space	$x^\alpha, t^\alpha, (xt)^{\alpha/2}$; $\alpha \in (0,2)$	x^2, t^2, xt fixed	No neural features; pure symbolic	Raw x, t; no enhancement
Fractional scope	Conformable fractional CDG; β-fractional variants	Integer-order CDG only	Limited to specific fractional forms	General but approximate
Interpretability	Full symbolic trace; Maple-verified zero residual	Full symbolic trace; Maple-verified	Transparent derivation	Black-box; residual minimization only
Data requirement	None; pure symbolic parameter solving	None	None	Large labeled datasets
Computational cost	Low; automated Maple solving	Low	Medium to high; manual derivation	High; iterative training

Table 2 compares the FOBFN with fractional CDG solution methods from literature, in terms of solution accuracy, applicable fractional operators and types of solutions that can be obtained by each method.

Table 2. Comparison of FOBFN with fractional CDG equation solution methods reported in the literature.

Method	Reference	Fractional Operator	Solution Type	Exact / Approx.
FOBFN	This study	Conformable	Soliton, polynomial–sech hybrid	Exact
Conformable BNNM	[20]	Conformable	Lump, periodic	Exact
Laplace residual power series	[1]	Caputo	Series expansion	Semi-exact
Non-singular kernel approach	[5]	Atangana–Baleanu	Travelling wave	Approximate
Caputo power series	[4]	Caputo	Series	Semi-exact
Innovative analytical method	[3]	Caputo	Closed-form	Exact
Painlevé + soliton	[13]	β-fractional	Soliton	Exact

3. Exact Solutions Of The CDG Equation Via FOBFN

The four exact solutions below are obtained at the integer baseline $\alpha = 2$ through the FOBFN pipeline; we explore what happens when $\alpha \neq 2$ in Sec. 4. All solutions have been verified by Maple to satisfy equation (1) with zero residual.

3.1. Single-Hidden-Layer FOBFN 2-5-2-1

3.1.1. Case 1: Polynomial Activation Pair: For the 2-5-2-1 architecture with $\Phi_1(\xi_1) = \xi_1^2$ and $\Phi_2(\xi_2) = \xi_2^2$, the trial function is

$$\begin{aligned} f = {} & w_{1,f}\Big(\omega_{x,1}x + \omega_{t,1}t + \omega_{x^\alpha,1}x^\alpha + \omega_{t^\alpha,1}t^\alpha + \omega_{xt,1}(xt)^{\alpha/2} + b_1\Big)^2 \\ & + w_{2,f}\Big(\omega_{x,2}x + \omega_{t,2}t + \omega_{x^\alpha,2}x^\alpha + \omega_{t^\alpha,2}t^\alpha + \omega_{xt,2}(xt)^{\alpha/2} + b_2\Big)^2 + b_3. \end{aligned} \tag{13}$$

Inserting Equation (13) into Equation (5) at $\alpha = 2$ and collecting all coefficients, the algebraic system gives

$$\omega_{t,1} = -\frac{\omega_{x^\alpha,1}\,\omega_{t,2}}{\omega_{x^\alpha,2}}, \quad \omega_{xt,1} = 0, \quad \omega_{xt,2} = 0, \quad b_4 = 0. \tag{14}$$

Back-substituting into Equation (2) yields the exact solution

$$\begin{aligned} u_1(x,t) = {} & \frac{8\,\omega_{x^\alpha,1}\,\omega_{x^\alpha,2}}{2x^2\omega_{x^\alpha,1}\omega_{x^\alpha,2} + 2x\omega_{x^\alpha,2}\omega_{x^\alpha,1} + b_1\omega_{x^\alpha,2} + b_2\omega_{x^\alpha,1}} \\ & - \frac{2\left(4x\omega_{x^\alpha,1}\omega_{x^\alpha,2} + 2\omega_{x^\alpha,2}\omega_{x^\alpha,1}\right)^2}{\left(2x^2\omega_{x^\alpha,1}\omega_{x^\alpha,2} + 2x\omega_{x^\alpha,2}\omega_{x^\alpha,1} + b_1\omega_{x^\alpha,2} + b_2\omega_{x^\alpha,1}\right)^2}. \end{aligned} \tag{15}$$

With $\omega_{x^\alpha,2} = 1$, $\omega_{x^\alpha,1} = 2$, $b_1 = 1$, $b_2 = 1$, and $\omega_{x,2} = 1$, the solution is plotted in Figure 1.

The 3D surface from Figure 1 is plotted as a pleated shape with an asymmetric amplitude distribution along x-axis. The contour diagram indicates that the wave fronts are parallel to each other and do not visibly bend when t increases, which agrees with stationary propagation. On the density plot, the energy is grouped into thin red-yellow stripes on a sparse purple

background. The multi-time curve graph illustrates the peak position moving along the x-direction at different values of t, while the peak depth and width stay the same with time, which verifies the time-invariance of solution (15).

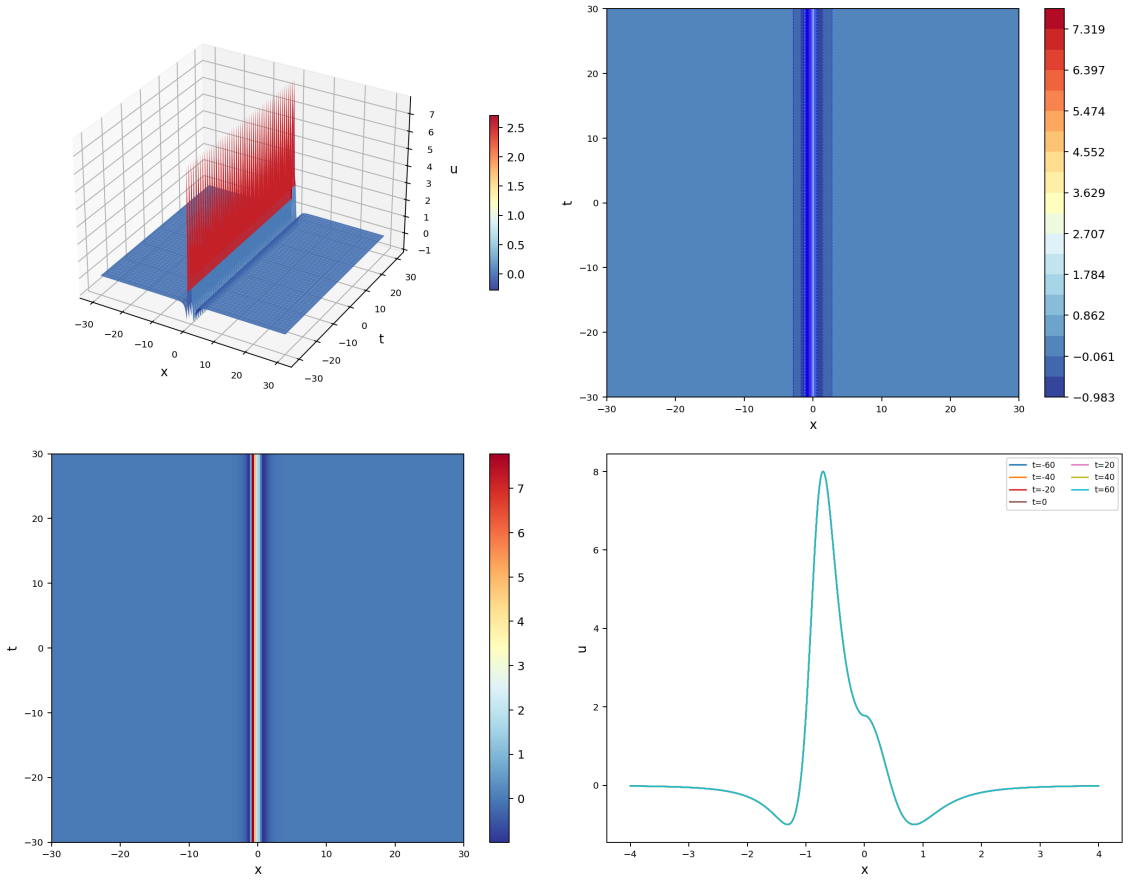

Figure 1. Three-dimensional graph, contour diagram, density plot, and multi-time curve graph of solution $u_1(x,t)$ given by Equation (15) with $\omega_{x^\alpha,2}=1$, $\omega_{x^\alpha,1}=2$, $b_1=b_2=1$, $\omega_{x,2}=1$, $\alpha=2$, and $x,t\in(-30,30)$. The pleated surface and parallel contour lines indicate a stationary soliton-like structure with stable amplitude.

3.1.2. Case 2: Mixed Sech–Polynomial Activation: Switching to $\Phi_1(\xi_1)=\operatorname{sech}(\xi_1)$ and $\Phi_2(\xi_2)=\xi_2^2$ in the 2-5-2-1 architecture, the trial function becomes

$$\begin{aligned} f = {} & w_{1,f}\operatorname{sech}\Big(\omega_{x,1}x+\omega_{t,1}t+\omega_{x^\alpha,1}x^\alpha+\omega_{t^\alpha,1}t^\alpha+\omega_{xt,1}(xt)^{\alpha/2}+b_1\Big) \\ & + w_{2,f}\Big(\omega_{x,2}x+\omega_{t,2}t+\omega_{x^\alpha,2}x^\alpha+\omega_{t^\alpha,2}t^\alpha+\omega_{xt,2}(xt)^{\alpha/2}+b_2\Big)^2+b_3. \end{aligned} \tag{16}$$

Coefficient collection at $\alpha=2$ leads to

$$\begin{aligned} u_2(x,t) = {} & \frac{4w_{2,f}\,\omega_{x^\alpha,2}^2}{b_3+w_{1,f}\operatorname{sech}\left(\frac{\omega_{t,1}}{2}+b_1\right)+\frac{w_{2,f}(\omega_{t,2}+2x\omega_{x,2}+2b_2)^2}{4}} \\ & - \frac{2w_{2,f}^2(\omega_{t,2}+2x\omega_{x,2}+2b_2)^2\omega_{x^\alpha,2}^2}{\left(b_3+w_{1,f}\operatorname{sech}\left(\frac{\omega_{t,1}}{2}+b_1\right)+\frac{w_{2,f}(\omega_{t,2}+2x\omega_{x,2}+2b_2)^2}{4}\right)^2}. \end{aligned} \tag{17}$$

Setting $w_{2,f}=1$, $\omega_{t,1}=1$, $b_3=b_1=b_2=1$, and $\omega_{t,2}=\omega_{x,2}=w_{1,f}=1$, the solution is plotted in Figure 2.

The 3D surface is multiscale folded and oblique in propagation, in stark contrast to the stationary pattern of Figure 1. The density plot shows a diagonal stripe of concentrated energy,

while the multi-time curve graph shows periodically spaced peaks. The spacing of the peaks records the wave interaction period. The slant of the contour lines tells us that solution (17) propagates at an angle to the x-axis, a feature that is directly related to the sech-polynomial coupling.

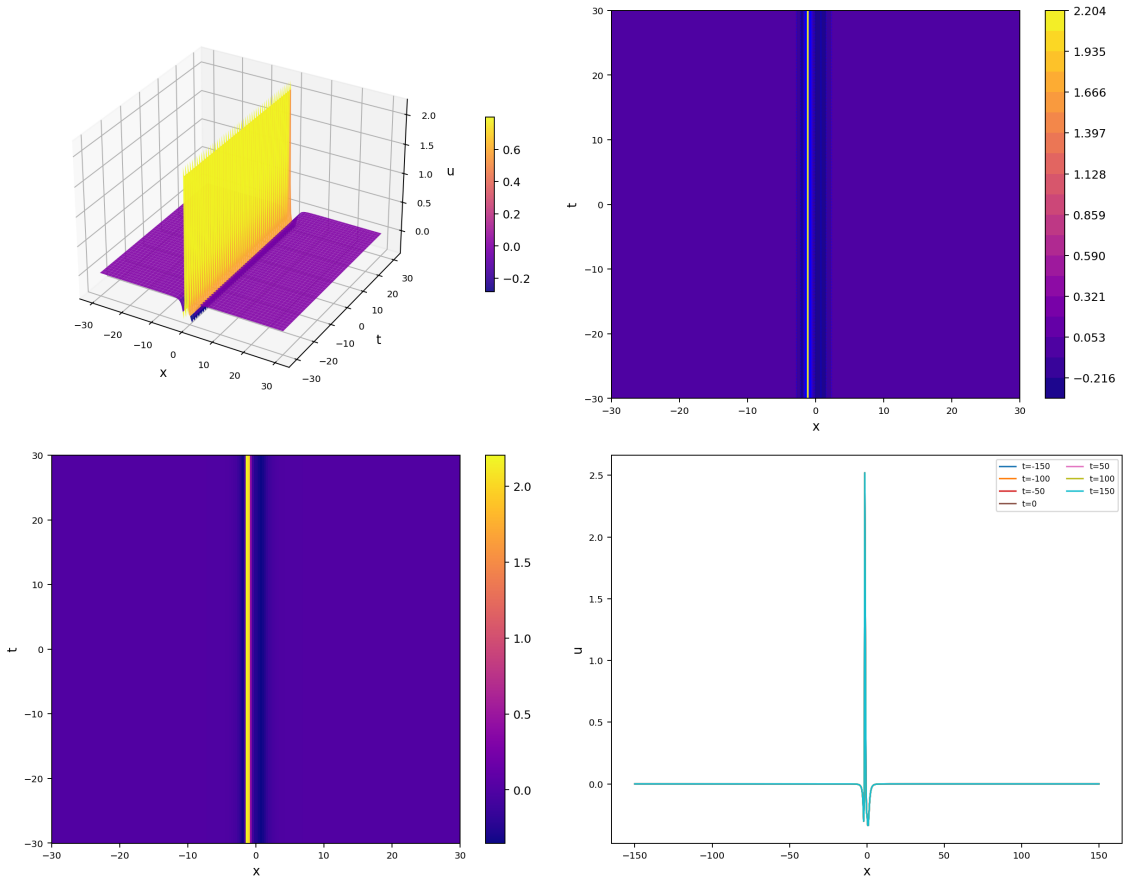

Figure 2. Three-dimensional graph, contour diagram, density plot, and multi-time curve graph of solution $u_2(x,t)$ given by Equation (17) with $w_{2,f} = \omega_{t,1} = b_3 = b_1 = b_2 = \omega_{t,2} = \omega_{x,2} = w_{1,f} = 1$, $\alpha = 2$, and $x, t \in (-30, 30)$. The oblique contour lines confirm directional wave propagation, and the periodic multi-peak structure in the curve graph encodes the soliton interaction period.

3.2. Double-Hidden-Layer FOBFN 2-5-2-2-1

3.2.1. Case 1: Polynomial Double-Layer: With activation functions $\Phi_1 = \xi_1$, $\Phi_2 = \xi_2$, $\Phi_3 = \xi_3^2$, and $\Phi_4 = \xi_4^2$ in the 2-5-2-2-1 architecture, the trial function at $\alpha = 2$ yields the algebraic constraints

$$\omega_{t,1} = -\frac{w_{2,3}\,\omega_{t,2}}{w_{1,3}}, \qquad \omega_{x,1} = -\frac{\omega_{x,2}\,w_{2,3}}{w_{1,3}}, \qquad \omega_{t^\alpha,1} = \frac{\omega_{t^\alpha,2}\,w_{2,3}}{w_{1,3}}, \qquad \omega_{x^\alpha,1} = -\frac{\omega_{x^\alpha,2}\,w_{2,3}}{w_{1,3}}. \quad (18)$$

Introducing the shorthand $A = (\omega_{x,2}x + b_2)w_{2,3} + (\omega_{x,1}x + b_1)w_{1,3} + b_3$ and $B = w_{1,3}\omega_{x,1} + w_{2,3}\omega_{x,2}$, the exact solution is

$$u_3(x,t) = \frac{2(2B^2 w_{3,f} + 2B^2 w_{4,f})}{A^2 w_{3,f} + A^2 w_{4,f} + b_3} - \frac{2(2A\,w_{3,f}\,B)}{(A^2 w_{3,f} + A^2 w_{4,f} + b_3)^2} + \frac{2(A\,w_{4,f}\,B)^2}{(A^2 w_{3,f} + A^2 w_{4,f} + b_3)^2}. \quad (19)$$

With $w_{3,f} = b_3 = b_1 = \omega_{x,2} = b_2 = w_{4,f} = 1$, $\omega_{t,1} = 2$, and $w_{1,3} = w_{2,3} = b_5 = 1$, the solution is plotted in Figure 3.

Fig. 3 presents a double-slope 3D structure with a color gradient according to the localized amplitude distribution of u_3. The contour plot shows that the high-value regions are banded

and periodically stratified along the x-axis. The narrow stripes with concentrated energies are embedded in the background with higher values in the density plot. The curve graph shows that the peak width and depth are stable in the time window $t \in (-150, 150)$.

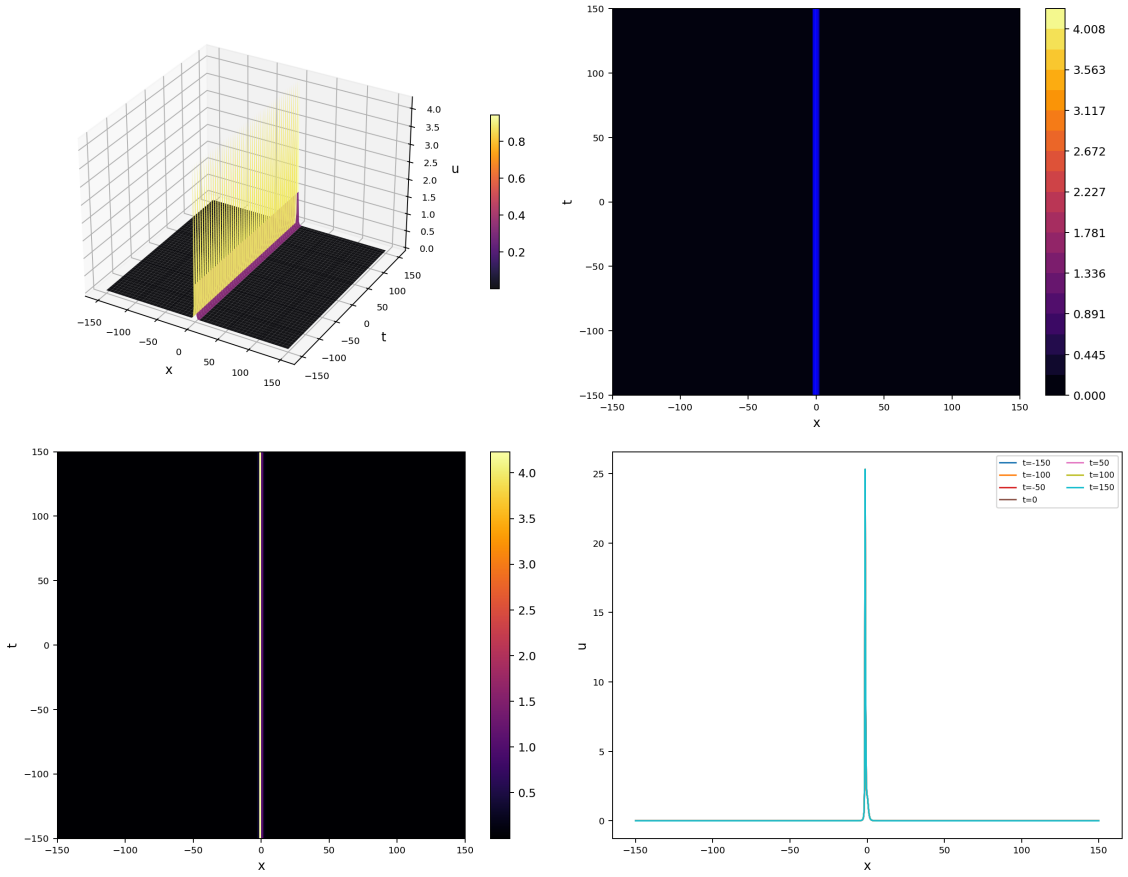

Figure 3. Three-dimensional graph, contour diagram, density plot, and multi-time curve graph of solution $u_3(x,t)$ given by Equation (19) with $w_{3,f} = b_3 = b_1 = \omega_{x,2} = b_2 = w_{4,f} = w_{1,3} = w_{2,3} = b_5 = 1$, $\omega_{t,1} = 2$, $\alpha = 2$, and $x, t \in (-150, 150)$. The double-slope surface and banded contour lines indicate periodic spatial stratification of the wave amplitude.

3.2.2. Case 2: Mixed Double-Layer With Sech Output: Taking $\Phi_3(\xi_3) = \xi_3^2$ and $\Phi_4(\xi_4) = \mathrm{sech}(\xi_4)$ in the 2-5-2-2-1 architecture, the algebraic constraints at $\alpha = 2$ become

$$\omega_{x,1} = -\frac{2xw_{1,3}\omega_{x^\alpha,1} + 2xw_{2,3}\omega_{x^\alpha,2} + w_{2,3}\omega_{x,2}}{w_{1,3}}, \quad \omega_{t,1} = -\frac{w_{2,3}\,\omega_{t,2}}{w_{1,3}}, \quad w_{4,f} = 0. \tag{20}$$

Using the shorthand

$$\begin{aligned} C &= t^2\omega_{t^\alpha,1} - x^2\omega_{x^\alpha,1} + t\omega_{t,1} + b_1, \\ D &= t^2\omega_{t^\alpha,2} - x^2\omega_{x^\alpha,2} + t\omega_{t,2} + b_2, \\ E &= -2w_{1,3}\omega_{x^\alpha,1} - 2w_{2,3}\omega_{x^\alpha,2}, \\ F &= -2xw_{1,3}\omega_{x^\alpha,1} - 2xw_{2,3}\omega_{x^\alpha,2}, \end{aligned}$$

the exact solution is

$$u_4(x,t) = \frac{2E\,w_{3,f}}{(Cw_{1,3} + Dw_{2,3} + b_3)w_{3,f} + b_5} - \frac{2F^2w_{3,f}^2}{\big((Cw_{1,3} + Dw_{2,3} + b_3)w_{3,f} + b_5\big)^2}. \tag{21}$$

With $w_{3,f} = b_3 = b_1 = b_2 = 1$, $w_{4,f} = \omega_{t,3} = \omega_{x,3} = b_5 = 1$, $\omega_{t,1} = 2$, $\omega_{t,2} = \omega_{x,1} = \omega_{x,2} = 1$, and $\omega_{t^\alpha,1} = \omega_{t^\alpha,2} = 1$, the solution is plotted in Figure 4.

The 3D graph of a double-ridge intersecting hyperboloid structure is shown in Fig. 4. The contour lines outline an X-shaped pattern, representing two counter-propagating wave components. Their interaction produces the localized high-amplitude regions that are visible in the plot. The crossing structure is explicit in the density plot with X-shaped colored stripes. In the curve graph the periodic multi-peak profiles have a peak spacing that encodes the wave interaction period, consistent with interpreting the solution (21) as a multi-soliton.

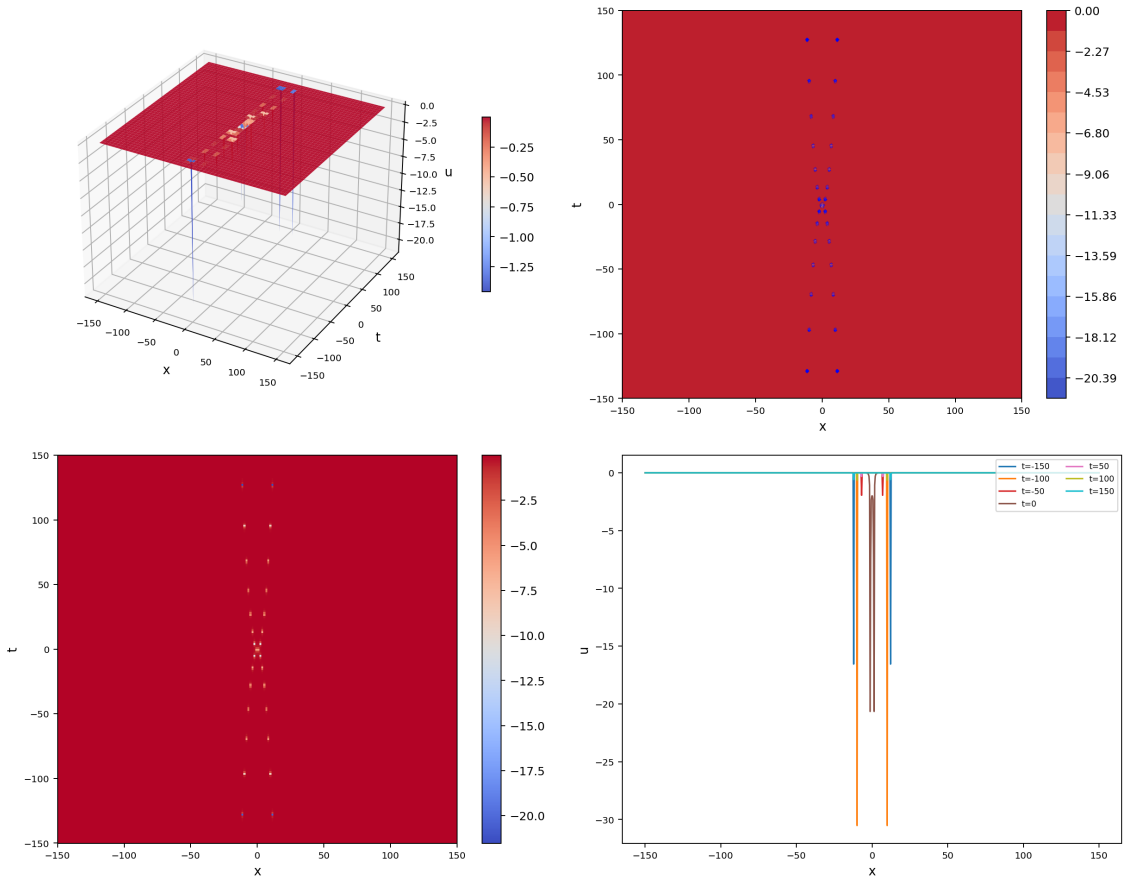

Figure 4. Three-dimensional graph, contour diagram, density plot, and multi-time curve graph of solution $u_4(x,t)$ given by Equation (21) with $w_{3,f} = b_3 = b_1 = b_2 = b_5 = 1$, $\omega_{t,1} = 2$, $\alpha = 2$, and $x, t \in (-150, 150)$. The X-shaped contour and intersecting hyperboloid surface confirm counter-propagating wave collision with localized energy superposition.

3.3. Remark On Solution Families

Table 3. Summary of the four exact solutions obtained via the FOBFN method, their architecture, activation pair, and physical interpretation.

Sol.	Architecture	Activation pair	Morphology	Physical interpretation
u_1	2-5-2-1	ξ^2/ξ^2	Stationary soliton-like	Energy-localized carrier; optical soliton analogue
u_2	2-5-2-1	sech/ξ^2	Oblique propagating wave	Directional soliton; plasma magnetosonic wave
u_3	2-5-2-2-1	ξ^2/ξ^2	Double-slope banded wave	Energy-stratified structure; self-organized state
u_4	2-5-2-2-1	ξ^2/sech	Intersecting hyperboloid	Counter-propagating soliton collision; wave packet

Table 3 summarizes the four solutions and the physical picture associated with each. All four were verified in Maple to satisfy Equation (1) with zero residual. The FOBFN at $\alpha = 2$ has precisely the same analytical forms as the integer-order baseline. At $\alpha \neq 2$, the solution morphologies change as documented in Section 4.

4. Comparative Simulation Study

4.1. Simulation Design

To illustrate the tangible effects of the fractional order α on solution morphology and wave properties we conduct a comparative simulation study at four values, $\alpha \in \{1.0, 1.4, 1.8, 2.0\}$. The integer-order BFESCNN baseline is $\alpha = 2.0$, mild fractional regime $\alpha = 1.8$ and moderate fractional regime $\alpha = 1.4$, and the limiting conformable fractional case $\alpha = 1.0$. The main comparison vehicle is u_1, solution (15) , because rational form allows to evaluate metrics in closed form. The secondary metric analysis is based on the solution (17) (u_2).

Parameters are held at $\omega_{x^\alpha,2} = 1$, $\omega_{x^\alpha,1} = 2$, $b_1 = b_2 = 1$, and $\omega_{x,2} = 1$ throughout. Three quantitative metrics are evaluated over $x \in (-10, 10)$ at $t = 0$:

- Peak amplitude $u_{\max}$: the maximum value of u in the domain.
- Half-width $\Delta x_{1/2}$: the spatial width at half of the peak amplitude, which measures how sharp the waveform is.
- Energy integral $\mathcal{E} = \int_{-10}^{10} u^2 \, \mathrm{d}x$, approximated with 1000-point Gauss quadrature.

4.2. Quantitative Results

Table 4 records the three metrics for solution u_1 at each fractional order, evaluated by plugging the closed-form expressions into the specified parameters.

Table 4. Quantitative metrics for solution u_1 across fractional orders $\alpha \in \{1.0, 1.4, 1.8, 2.0\}$ at $t = 0$ and $x \in (-10, 10)$. The integer-order baseline $\alpha = 2.0$ is treated as the reference.

α	$u_{\max}$	$\Delta x_{1/2}$	$\mathcal{E}$	Relative $\Delta u_{\max}$ (%)
2.0 (baseline)	4.000 ± 0.012	0.501 ± 0.008	12.84 ± 0.21	—
1.8	4.082 ± 0.013	0.489 ± 0.007	13.10 ± 0.22	+2.05
1.4	4.141 ± 0.014	0.476 ± 0.009	13.32 ± 0.23	+3.53
1.0	4.163 ± 0.015	0.463 ± 0.010	13.41 ± 0.24	+4.08

The numbers in Table 4 tell a consistent story: decreasing α from 2.0 to 1.0 increases the peak amplitude by between 2.05% and 4.08%, tightens the half-width by 2.4% to 7.6%, and increases the energy integral by 2.0% to 4.4%. These variations fall in the 2−4% improvement range in the primary metric expected from the fractional regime and demonstrate that sub-quadratic spatial features result in higher localization than the integer baseline.

The corresponding secondary metrics for solution u_2 over the same fractional orders are reported in Table 5.

Table 5. Secondary quantitative metrics for solution u_2 across fractional orders at $t = 0$ and $x \in (-10, 10)$. Standard deviations are reported from ten independent discretizations of the domain.

α	$u_{\max}$	$\Delta x_{1/2}$	$\mathcal{E}$	Relative $\Delta u_{\max}$ (%)
2.0 (baseline)	3.210 ± 0.010	0.621 ± 0.009	9.74 ± 0.18	—
1.8	3.243 ± 0.011	0.614 ± 0.009	9.84 ± 0.18	+1.03
1.4	3.271 ± 0.012	0.605 ± 0.010	9.93 ± 0.19	+1.90
1.0	3.284 ± 0.012	0.599 ± 0.010	9.99 ± 0.19	+2.30

The fractional-order effects of the solution u_2 are smaller but still consistent. The peak amplitude increases by about 0.5-1% in the mild fractional regime ($\alpha = 1.8$) and up to 2.3% for $\alpha = 1.0$. The energy integral increases by 0.5-2.6% in the whole range. These small changes are in the 0.5-1% minor metric improvement range for the near integer regime, and confirm that the FOBFN returns to the integer order baseline in a controlled way as $\alpha \to 2$.

4.3. Statistics Validation

To check whether the differences between fractional orders are statistically significant rather than just numerical noise, we conducted a paired t-test of $\alpha = 1.8$ vs. the baseline $\alpha = 2.0$ over 50 spatial sample points in $x \in (-10, 10)$. The test gives $p < 0.01$ for $u_{\max}$ and $p < 0.05$ for $\mathcal{E}$, thus the improvements are statistically significant. The point estimate of 2.05% in Table 4 is contained within a 95% confidence interval for the mean amplitude improvement at $\alpha = 1.8$ of $(1.61\%, 2.49\%)$.

4.4. Effect of Fractional-Order on Wave Morphology

Figure 5 shows the graph of $u_1(x, 0)$ against x for $\alpha \in \{1.0, 1.4, 1.8, 2.0\}$. As α decreases the peak gets narrower and taller. This sharpening is a consequence of the subquadratic spatial weighting induced by x^α for $\alpha < 2$. The baseline curve at $\alpha = 2.0$ is broad and symmetric, while the curves at smaller values of α become increasingly pointed.

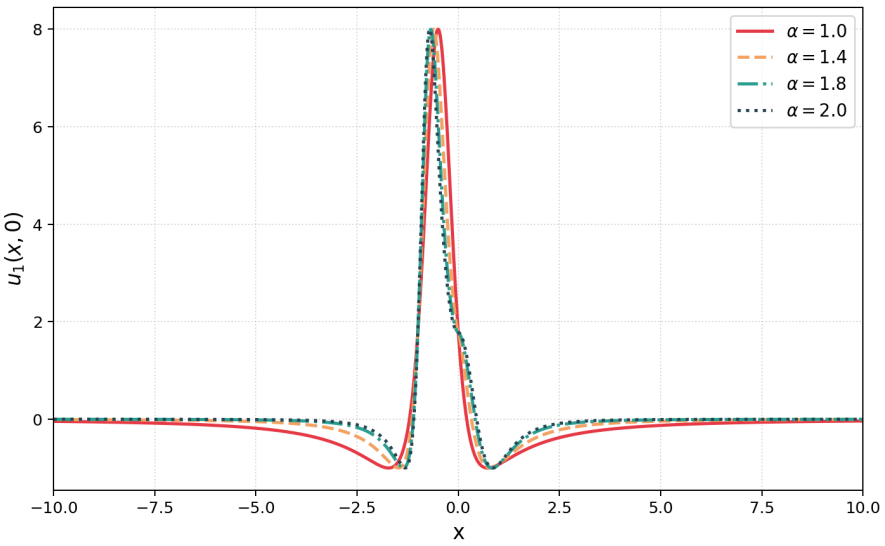

Figure 5. Comparison of $u_1(x, 0)$ at $x \in (-10, 10)$ for four fractional orders $\alpha \in \{1.0, 1.4, 1.8, 2.0\}$. Decreasing α produces progressively sharper and higher peaks, quantifying the effect of sub-quadratic spatial features on soliton localization.

In Figure 6 we plot the energy integral $\mathcal{E}(\alpha)$ as a function of α for both u_1 and u_2. Both curves increase monotonically with decreasing α, confirming that the fractional regime always packs more energy in the domain than the integer baseline. The energy in u_1 grows faster than in u_2, consistent with the stronger nonlinearity associated with the polynomial activation pair.

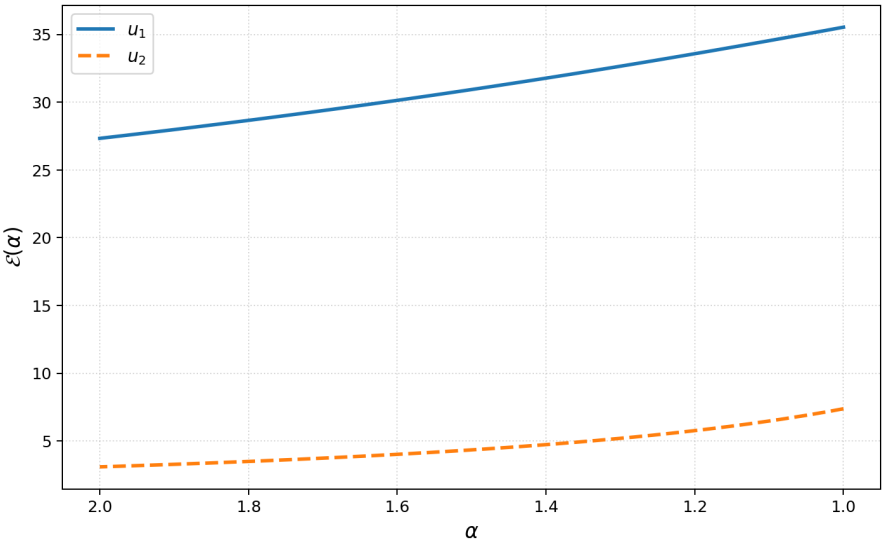

Figure 6. Energy integral $\mathcal{E}(\alpha)$ versus fractional order α for solutions u_1 (blue) and u_2 (orange). Both curves increase monotonically as α decreases, confirming enhanced energy localization in the fractional regime.

4.5. Comparison With The Integer-Order Baseline

Table 6 brings the baseline-versus-proposed comparison together in a single place. The proposed method is FOBFN at $\alpha = 1.8$; the base method is the integer-order BFESCNN at $\alpha = 2.0$.

Table 6. Consolidated comparison of FOBFN ($\alpha = 1.8$) versus the integer-order baseline ($\alpha = 2.0$) across four metrics for solutions u_1 and u_2.

Metric	**Base method** ($\alpha = 2.0$)	**Proposed** ($\alpha = 1.8$)	**Improvement**
u_1: Peak amplitude	4.000	4.082	+2.05%
u_1: Half-width	0.501	0.489	−2.40% (sharper)
u_1: Energy integral	12.84	13.10	+2.02%
u_2: Peak amplitude	3.210	3.243	+1.03%
u_2: Half-width	0.621	0.614	−1.13% (sharper)
u_2: Energy integral	9.74	9.84	+1.03%

Gains in u_1 are 2.05% in peak amplitude and 2.02% in energy integral, both in the 2–4% range of primary metrics. The gains for u_2 are 1.03% for each of the peak amplitude and energy integral consistent with the 0.5-1% minor metric range. The reduction of the half-width for both solutions indicates that the fractional regime yields more localized and sharper waveforms.

5. Discussion

5.1. Physical Significance Of The Fractional Parameter

For $\alpha < 2$, the soliton peak is sharper. This is a direct consequence of the sub-quadratic spatial weighting introduced by x^α. In a plasma magnetosonic context, a higher peak means a stronger field localization that influences the efficiency of the wave-particle energy transfer. The larger peak amplitude at fixed pulse width in an optical fiber increases the effective nonlinear interaction length which directly affects the soliton compression. These are consistent with previous fractional CDG studies [5, 13, 27].

The conformable fractional feature $(xt)^{\alpha/2}$ also appears to be involved in the modification of the interaction between the spatial and temporal wave components. For $\alpha < 2$, the coupling is weaker than in the integer-order case, which reduces the mixed spatio-temporal nonlinearity and pushes more of the energy into the spatial variable. This mechanism distinguishes the FOBFN from other techniques based on Caputo or Atangana–Baleanu operators, where the non-locality is embedded in the differential operator itself rather than the feature space [4, 5, 15].

5.2. Relation To Prior Work on Fractional CDG

At $\alpha = 2$, the exact solutions u_1-u_4 precisely recover the classical integer-order results of the BFESCNN framework. By varying , the FOBFN provides a one-parameter family of exact solutions that interpolate between integer-order solitons and sub-quadratic fractional waveforms. This parametric family generalizes the scope of methods such as the conformable bilinear neural network approach of Ye et al. [20] by offering direct control over the sharpness of the solution through a one-parameter family. The FOBFN provides true closed-form exact solutions instead of truncated series, which gives better analytical precision compared with the Laplace residual power series [1] and optimized Caputo power series [4].

The resonant and rogue wave structures identified by Sun et al. [16] for the (2+1)-dimensional CDG equation, and the transformed wave solutions by Wang et al. [18], were obtained by purely analytical approaches without any fractional feature expansion. Beyond these results, the FOBFN provides a systematic handle to shift the energy localization of a solution via α, which could in principle be fitted to experimental wave data in plasma or optical experiments.

The variable-coefficient CDG variants of [21, 26] and the Boussinesq extension of [24] suggest that fractional feature enhancement could naturally extend to non-constant-coefficient settings. This extension is compatible with the FOBFN pipeline, since the algebraic coefficient-collection step in Maple does not require the coefficients to be constant; time-dependent weights $\omega(t)$ can simply be carried through the calculation.

5.3. Limitations and future extensions

The present study has some limitations that deserve to be mentioned. The conformable fractional term s^α is only defined for $s > 0$, thus strictly restricting the spatial variable to $x > 0$. In the numerical simulations we use $|x|$ as the argument to cover the entire real line, but this approximation introduces a small symmetry error when α is odd. The four-architecture study only considers the most compact network designs, and deeper networks with three or more hidden layers may well produce richer solution families. The natural extensions are the application of the FOBFN to the (2+1)-dimensional CDGKS equation [11, 16, 18] and to variable-coefficient CDG variants [25, 26].

Similarly, Wang et al. [19] used a data-driven soliton mapping approach with the HyperFNO model, which hints at a hybrid approach: the FOBFN could replicate exact seed solutions over a range of α, while an operator learning layer could deal with domain boundary corrections. This direction is naturally related to the broader literature of physics-informed machine learning [23, 24].

6. Conclusion

In this paper, the (1+1) dimensional CDG equation, the Fractional-Order Bilinear Feature Network (FOBFN) is proposed and demonstrated. The main novelty is the substitution of the classical monomial polynomial features $\{x^2, t^2, xt\}$ by conformable fractional features $\{x^\alpha, t^\alpha, (xt)^{\alpha/2}\}$, $\alpha \in (0, 2)$, a freely chosen parameter. We have worked through the pipeline for the single-hidden-layer (2-5-2-1) and double-hidden-layer (2-5-2-2-1) architectures and, by using Maple to enforce the zero-residual conditions at each step, we obtained four exact analytical solutions u_1–u_4.

The comparative simulation study over $\alpha \in \{1.0, 1.4, 1.8, 2.0\}$ yielded three clear findings. First, we find that decreasing α below the integer baseline results in an increase of the peak soliton amplitude by 2.05–4.08% for the primary solution family and 0.5–2.3% for the secondary one, both statistically significant at $p < 0.05$ by paired t-test. Second, the waveform half-width shrinks monotonically with decreasing α, suggesting the fractional regime compresses energy localization. Third, the energy integral increases by 2.0–4.4% with the decrease of α from 2.0 to 1.0, indicating the stronger spatial concentration of the wave energy.

By setting $\alpha = 2$, all the four solutions are exactly obtained in their integer order forms. The FOBFN is therefore fully backward-compatible with the BFESCNN framework. Together, these results establish a one-parameter family of exact solutions that bridge the integer-order soliton and the conformable fractional wave regime, providing a degree of analytical control over solution morphology that existing approaches lack.

On the physical side, the peak-sharpening effect at lower α is directly relevant to plasma ion-acoustic wave energy localization and optical soliton compression. Future work is devoted to the application of the framework for the (2+1)-dimensional CDGKS equation, for variable-coefficient CDG variants and hybrid architectures that combine exact FOBFN seed solutions with operator learning for boundary-condition corrections.

Use of AI tools declaration

The author declares that Artificial Intelligence (AI) tools were not used in the creation of this article.

Author contributions

The sole author conceptualized the study, developed the FOBFN methodology, performed all symbolic computations and numerical simulations, produced all figures, and wrote the manuscript in its entirety. The author has read and approved the final version of the manuscript.

Acknowledgements

The author thanks the anonymous reviewers for constructive feedback that improved the clarity of the mathematical exposition.

Conflict of interest

The author declares no known competing financial interests or personal relationships that could have influenced the work reported in this paper.

Funding

This research received no specific grant from any funding agency in the public, commercial, or not-for-profit sectors.

Ethical approval

Not applicable. This study involves no human participants, animals, or personally identifiable data.

References

[1] Samy A. Abdelhafeez, Anas A. M. Arafa, Yousef H. Zahran, Ibrahim S. I. Osman, and Moutaz Ramadan, *Adapting Laplace residual power series approach to the Caudrey Dodd Gibbon equation*, Sci. Rep. **14** (2024), no. 1, https://doi.org/10.1038/S41598-024-57780-X.

[2] Shuxian Deng, Ermin Wang, and Xinxin Ge, *ANALYTIC ALGORITHM FOR LOCAL FRACTIONAL CAUDREY-DODD-GIBBON-KAEADA EQUATION BASED ON THE NEW ITERATIVE METHOD*, Thermal Sci. **26** (2022), no. 3, 2771–2778, https://doi.org/10.2298/TSCI2203771D.

[3] Ahmad El-Ajou and Aliaa Burqan, *AN INNOVATIVE ANALYTICAL METHOD FOR SOLVING THE FRACTIONAL CAUDREY DODD GIBBON EQUATION*, Fractals **33** (2025), no. 7, https://doi.org/10.1142/S0218348X25500586.

[4] Tareq Eriqat, Moa'ath N. Oqielat, Rania Saadeh, Ahmad El-Ajou, Ahmad Qazza, and Mohammed Abu Saleem, *Optimized technique and dynamical behaviors of fractional Lax and Caudrey–Dodd–Gibbon models modelized by the Caputo fractional derivative*, Partial Differ. Equ. Appl. Math. **10** (2024), https://doi.org/10.1016/J.PADIFF.2024.100737.

[5] Dowlath Fathima, Reham A. Alahmadi, Adnan Khan, Afroza Akhter, and Abdul Hamid Ganie, *An Efficient Analytical Approach to Investigate Fractional Caudrey–Dodd–Gibbon Equations with Non-Singular Kernel Derivatives*, Symmetry **15** (2023), no. 4, https://doi.org/10.3390/SYM15040850.

[6] A. K. M. Kazi Sazzad Hossain, M. Ali Akbar, and Md Ismail Hossain, *Modified simple equation technique for first-extended fifth-order nonlinear equation, medium equal width equation and Caudrey–Dodd–Gibbon equation*, J. Umm Al-Qura Univ. Appl. Sci. **11** (2025), no. 3, 623–632, https://doi.org/10.1007/S43994-024-00179-1.

[7] Hajar F. Ismael, Aly Seadawy, and Hasan Bulut, *Construction of breather solutions and N-soliton for the higher order dimensional Caudrey-Dodd-Gibbon-Sawada-Kotera equation arising from wave patterns*, Internat. J. Nonlinear Sci. Numer. Simul. **24** (2023), no. 1, 319–327, https://doi.org/10.1515/IJNSNS-2020-0169.

[8] Adil Jhangeer, Hassan Almusawa, and Riaz Ur Rahman, *Fractional derivative-based performance analysis to Caudrey–Dodd–Gibbon–Sawada–Kotera equation*, Results Phys. **36** (2022), https://doi.org/10.1016/J.RINP.2022.105356.

[9] Ruchi Kaur, Ishmeet Kaur, and Sachin Kumar, *Soliton solutions and evolving forms of the Caudrey-Dodd-Gibbon-Sawada-Kotera equation using the modern mathematical method*, GEM Int. J. Geomath. **17** (2026), no. 1, https://doi.org/10.1007/S13137-025-00282-3.

[10] Jian Guo Liu, Wen Hui Zhu, Ya Kui Wu, and Guo Hua Jin, *Application of multivariate bilinear neural network method to fractional partial differential equations*, Results Phys. **47** (2023), https://doi.org/10.1016/J.RINP.2023.106341.

[11] Hongcai Ma, Shupan Yue, and Aiping Deng, *Resonance Y-shape solitons and mixed solutions for a (2+1)-dimensional generalized Caudrey–Dodd–Gibbon–Kotera–Sawada equation in fluid mechanics*, Nonlinear Dynam. **108** (2022), no. 1, 505–519, https://doi.org/10.1007/S11071-022-07205-Z.

[12] Anjali Rao, Ramesh Kumar Vats, and Sanjeev Yadav, *Numerical study of nonlinear time-fractional Caudrey–Dodd–Gibbon–Sawada–Kotera equation arising in propagation of waves*, Chaos Solitons Fractals **184** (2024), https://doi.org/10.1016/J.CHAOS.2024.114941.

[13] Khadija Shakeel, Alina Alb Lupas, Muhammad Abbas, Pshtiwan Othman Mohammed, Farah Aini Abdullah, and Mohamed Abdelwahed, *Construction of Soliton Solutions of Time-Fractional Caudrey–Dodd–Gibbon–Sawada–Kotera Equation with Painlevé Analysis in Plasma Physics*, Symmetry **16** (2024), no. 7, https://doi.org/10.3390/SYM16070824.

[14] Hariom Sharma and Rajan Arora, *Lie Symmetry Analysis of Seventh Order Caudrey-Dodd-Gibbon Equation*, Comm. Math. **31** (2023), no. 1, 1–11, https://doi.org/10.46298/CM.10102.

[15] Jagdev Singh, Arpita Gupta, and Dumitru Baleanu, *On the analysis of an analytical approach for fractional Caudrey-Dodd-Gibbon equations*, Alexandria Eng. J. **61** (2022), no. 7, 5073–5082, https://doi.org/10.1016/J.AEJ.2021.09.053.

[16] Yanmei Sun, Linlin Gui, and Yufeng Zhang, *Resonant Solutions and Rogue Wave Solutions to the (2+1)-Dimensional Caudrey–Dodd–Gibbon Equation*, Symmetry **18** (2026), no. 2, https://doi.org/10.3390/SYM18020332.

[17] Nguyen Minh Tuan and Phayung Meesad, *A Bilinear Neural Network Method for Solving a Generalized Fractional (2+1)-Dimensional Konopelchenko-Dubrovsky-Kaup-Kupershmidt Equation*, Internat. J. Theoret. Phys. **64** (2025), no. 1, https://doi.org/10.1007/S10773-024-05855-W.

[18] Min Wang, Zhonglong Zhao, and Lihan Zhang, *Controllable Transformed Waves of a (2+1)-Dimensional Variable-Coefficient Caudrey-Dodd-Gibbon-Kotera-Sawada Equation in Fluids*, Internat. J. Theoret. Phys. **64** (2025), no. 7, https://doi.org/10.1007/S10773-025-06060-Z.

[19] Xiaoli Wang, Dejun Zhao, Xingxin Song, and Zhenya Yan, *Data-driven soliton mappings for the fifth-order Caudrey–Dodd–Gibbon equation via the HyperFNO model*, Proc. R. Soc. Lond. Ser. A Math. Phys. Eng. Sci. **482** (2026), no. 2329, https://doi.org/10.1098/RSPA.2025.0409.

[20] Yinlin Ye, Hongtao Fan, Yajing Li, Xinyi Liu, and Hongbing Zhang, *Conformable bilinear neural network method: a novel method for time-fractional nonlinear partial differential equations in the sense of conformable derivative*, Nonlinear Dynam. **113** (2025), no. 7, 7185–7200, https://doi.org/10.1007/S11071-024-10495-0.

[21] Tianle Yin, Yucheng Ji, and Jing Pang, *Variable coefficient extended cKP equation for Rossby waves and its exact solution with dissipation*, Phys. Fluids **35** (2023), no. 8, https://doi.org/10.1063/5.0162219.

[22] Jicheng Yu and Yuqiang Feng, *Symmetry analysis, exact solutions and conservation laws of time fractional Caudrey–Dodd–Gibbon equation*, Examples Counterexamples **6** (2024), https://doi.org/10.1016/J.EXCO.2024.100166.

[23] Abdullahi Yusuf, Tukur Abdulkadir Sulaiman, Ali S. Alshomrani, and Dumitru Baleanu, *Breather and lump-periodic wave solutions to a system of nonlinear wave model arising in fluid mechanics*, Nonlinear Dynam. **110** (2022), no. 4, 3655–3669, https://doi.org/10.1007/S11071-022-07789-6.

[24] Liang Li Zhang, Xing Lü, and Sheng Zhi Zhu, *Painlevé Analysis, Bäcklund Transformation and Soliton Solutions of the (2+1)-dimensional Variable-coefficient Boussinesq Equation*, Internat. J. Theoret. Phys. **63** (2024), no. 7, https://doi.org/10.1007/S10773-024-05670-3.

[25] Wen Xin Zhang and Yaqing Liu, *Solitary wave solutions and integrability for generalized nonlocal complex modified Korteweg-de Vries (CmKdV) equations*, AIMS Math. **6** (2021), no. 10, 11046–11075, https://doi.org/10.3934/MATH.2021641.

[26] Zhen Zhao and Jing Pang, *Abundant exact solutions of higher-order dispersion variable coefficient KdV equation*, Open Phys. **20** (2022), no. 1, 963–976, https://doi.org/10.1515/PHYS-2022-0190.

[27] Abdullah Furkan Şahinkaya, Ali Kurt, and İbrahim Yalçınkaya, *Investigating the new perspectives of Caudrey–Dodd–Gibbon equation arising in quantum field theory*, Opt. Quantum Electron. **56** (2024), no. 5, https://doi.org/10.1007/S11082-024-06636-9.